Picoseconds-Limited Exciton Recombination in Metal-Organic Chalcogenides Hybrid Quantum Wells

Picoseconds-limited exciton recombination in metal-organic chalcogenides hybrid quantum wells

Christoph Kastl[†§*], Adam M. Schwartzberg[†*], and Lorenzo Maserati[†‡*]

† The Molecular Foundry, Lawrence Berkeley National Laboratory, Berkeley, California 94720, USA.

§ Walter Schottky Institute and Physik Department, Technical University of Munich, Garching 85748, Germany.

‡ Center for Nano Science and Technology @PoliMi, Istituto Italiano di Tecnologia, 20133 Milan, Italy.

AUTHOR INFORMATION

Corresponding Authors

* christoph.kastl@wsi.tum.de, amschwartzberg@lbl.gov, lmaserati@lbl.gov.

ABSTRACT

Metal-organic species can be designed to self-assemble in large-scale, atomically defined, supramolecular architectures. A particular example are hybrid quantum wells, where inorganic two-dimensional (2D) planes are separated by organic ligands. The ligands effectively form an intralayer confinement for charge carriers resulting in a 2D electronic structure, even in multilayered assemblies. Air-stable layered transition metal organic chalcogenides have recently been found to host tightly bound 2D excitons with strong optical anisotropy in a bulk matrix. Here, we investigate the excited carrier dynamics in the prototypical metal organic chalcogenide $[AgSePh]_\infty$, disentangling three excitonic resonances by low temperature transient absorption spectroscopy. Our analysis suggests a complex relaxation cascade comprising ultrafast screening and renormalization, inter-exciton relaxation, and self-trapping of excitons within a few picoseconds. The ps-decay provided by the self-trapping mechanism may be leveraged to unlock the material's potential for ultrafast optoelectronic applications.

KEYWORDS: 2D excitons, Hybrid quantum wells, Metal-organic chalcogenides, Nanomaterials

Introduction

Atomically thin, inorganic semiconductors have gained enormous research interest as a test bench for room temperature manipulation of two-dimensional (2D) Wannier excitons.[1] Semiconductor hybrid quantum wells, such as metal-organic chalcogenides (MOCs) or metal halide perovskites,[2,3] show similar 2D excitons with binding energies up to hundreds of meV. In these hybrid materials, the inorganic planes are spaced by organic ligands, which provide a low dielectric screening environment and quantum confinement for the charge carriers. Due to the low dielectric screening, the optical properties are dominated by strongly bound exciton complexes.[4] This marks a stark contrast to all-inorganic quantum wells (e.g. III-V semiconductors-based), where both the insulating barriers and the active layers have high dielectric constants and diminish the exciton binding to few meV, restricting excitonic phenomena to cryogenic temperatures.[5] Hybrid, multilayered structures open an avenue for combining the chemical tunability of organic chemistry, bulk materials suitable for thin film technologies, and the advantageous (opto-)electronic properties of low-dimensional inorganic materials. This innovative concept of hybrid materials with strong excitonic character is rapidly emerging from the converging fields of metal-organic frameworks,[6,7] metal-organic coordination polymers,[8] and reduced dimensionality perovskites.[2] While two-dimensional metal halide perovskites are regarded as particularly appealing proof-of-concept, their applicability remains limited, because their ionic lattice is critically affected under standard operating conditions.[3] Air-stable MOCs with covalent character constitute an alternative for providing a hybrid quantum well platform for next generation optoelectronics.[4,9] So far, tens of different MOCs featuring quantum wire and quantum well nanostructures,[10–18] potentially hosting low-dimensional physics phenomena, were reported. However, research on this platform has focused on crystallographic and structural aspects, while the optoelectronic properties have been largely unexplored, with notable exceptions.[13–18]

An atomistic representation of $[AgSePh]_\infty$ (silver benzeneselenolate), a prototypical layered MOC, is shown in Fig. 1a. Its structure appears as a stack of inorganic/organic layers, with a periodicity of ~14 Å along the out-of-plane direction. Similar to layered transition metal chalcogenides, the individual layers are only weakly bound in the out-of-plane direction (*c*-axis) by van der Waals-type interactions between the benzene functional groups. Although the crystal structure was known for almost two decades,[19] its optical and electronic properties were only recently elucidated.[4,9,20] $[AgSePh]_\infty$ is a direct gap semiconductor with large optical anisotropy both between the out-of-plane *c*-axis and the in-plane *ab*-axes, as well as strong anisotropy within the *ab*-plane.[4] The optical absorption is dominated by tightly bound intralayer excitons confined within the 2D silver-selenide planes. At room temperature, the main excitonic transitions occur at 2.672 eV (464 nm, X_1), 2.738 eV (453 nm, X_2) and 2.870 eV (432 nm, X_3), and the single particle gap was determined to be 3.05 eV (407 nm) corresponding to an exciton binding energy of 380 meV, for the lowest excitation X_1.[4,20] A recent study investigated the excitonic fine structure via linear and non-linear photoluminescence excitation spectroscopy, adding several dark states as well as a subgap luminescence at low-temperatures to the picture.[20] From the time-resolved luminescence decay, an excited state lifetime on the order of 20 ps was deduced, although the origin of the fast luminescence decay was not determined.[20]

Here, we use ultrafast, broadband transient absorption spectroscopy to unravel the excited state dynamics in $[AgSePh]_\infty$ from femtoseconds to nanoseconds. We find a complex relaxation cascade involving screening and band-gap renormalization, inter-excitonic relaxation, trapping of excitons, and non-radiative coupling to the phonon bath. As the main finding, we show that fast self-trapping of charge carriers and/or excitons governs the timescales below 10 ps. Carrier trapping is of central importance for the utilization of excitonic materials in optoelectronics. While for energy conversion processes trapping is usually considered detrimental,[21] it can open new pathways for utilizing low-dimensional materials, and in particular $[AgSePh]_\infty$, for example as ultrafast optical switches, high-bandwidth detectors, or broadband pulsed light sources.[22,23]

Results

Thin films were prepared on quartz substrates by a chemical vapor–solid reaction yielding films with the *ab*-plane oriented mostly parallel to the substrate.[4,24] Due to the nanocrystalline morphology (grain size ~200 nm), the in-plane anisotropy was not relevant for all following experiments (spot sizes ~150 µm). Figure 1b displays steady state absorbance spectra of a 70 nm thin film from room temperature to 77 K. At low temperatures, the absorbance peaks significantly narrow, and the three excitons X_1, X_2, and X_3 can clearly be discerned. Additionally, an onset feature develops at 3.13 eV (396 nm) close to the energy of the single-particle gap at room temperature.[4,20] The transient absorption spectrum (Fig. 1c) also reveals these three resonances directly after optical excitation. The measurements were done in a transmission geometry, and we report the transient change in transmission $-\Delta T/T$. The latter corresponds approximately to the change in absorption, when neglecting interference and reflection effects for very thin films on transparent substrates.[25] Figure 1d shows the broadband transient absorption dynamics at a temperature of T = 77 K for an excitation wavelength of 3.758 eV (330 nm). As will be discussed in the following, the main transient changes of the excitonic resonances can be understood by ultrafast ground state depletion as well as bandgap renormalization due to the excited ensemble on short time scales (t < 0.5 ps), and by a heated phonon bath on long time scales (t ~ 100 ps). The decay of the excitonic features on intermediate time scales (t < 10 ps) is accompanied by the emergence of a broad, sub-gap photoinduced absorption (PIA), as emphasized by the adjusted color scale in Fig. 1d. While in steady-state absorption such a sub-gap feature is absent, low-temperature luminescence clearly shows a corresponding broadband emission near 600 nm (Supplementary Fig. S1). Since the excitonic decay matches closely the rise of the PIA (Fig. 1e), we assign the PIA to absorption from a trapped state populated by the decay of the exciton ensemble. Trapping can be relevant both for free carriers, i.e. the electron and/or hole are trapped independently, or excitons, i.e. the bound electron-hole pair is trapped directly.[21] The microscopic mechanism is often mediated by defects (extrinsic trapping).[26] For soft lattice configurations, as is the case for layered $[AgSePh]_\infty$, so-called intrinsic self-trapping can often become particularly relevant.[27] Then, the localization of the charge carrier or exciton at the trapping site induces a lattice deformation or even, in some cases, a reconfiguration of the local bonds,[28–30] providing a deep potential well for the localized state.

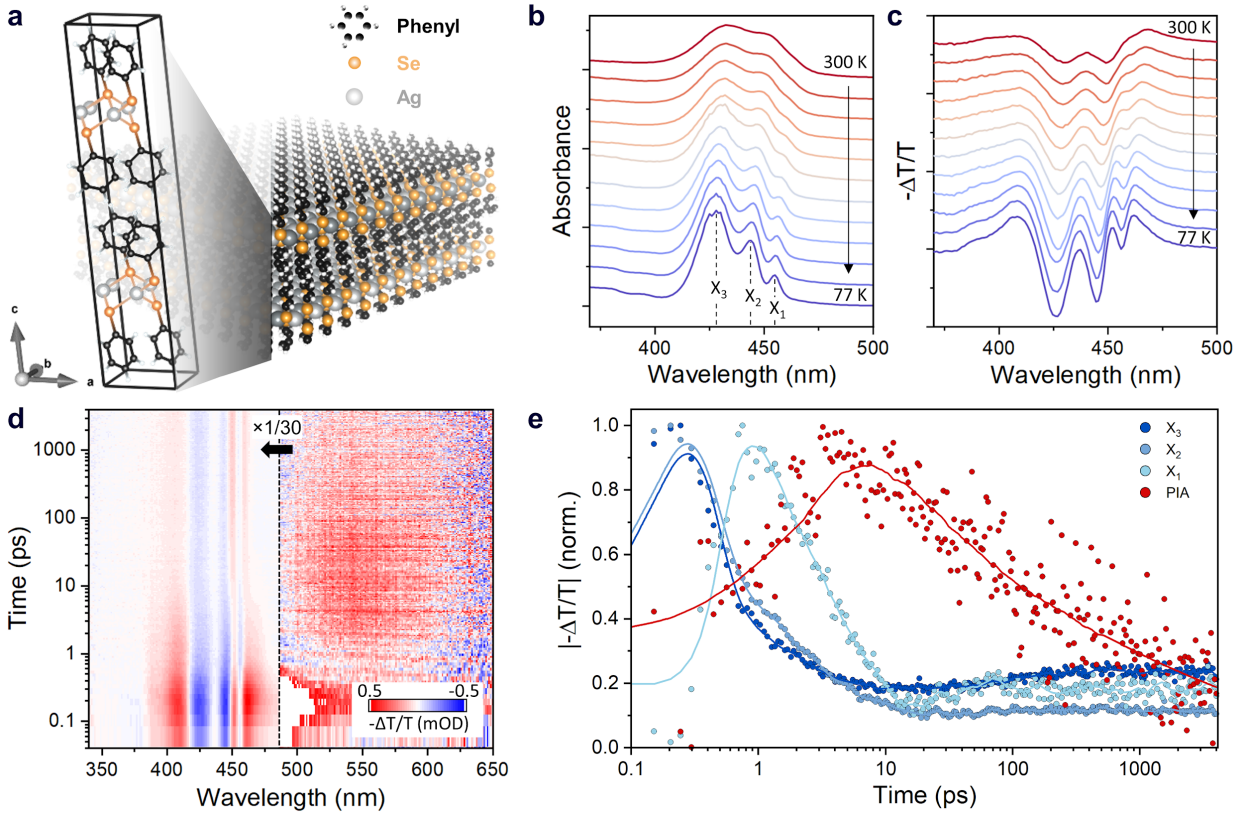

Figure 1a, Atomistic representation of $[AgSePh]_\infty$. **b,** Thin film absorption spectra and **c,** transient absorption spectra directly after pump excitation (330 nm wavelength) from room temperature down to 77 K. The three main excitonic resonances are labelled X_1, X_2 and X_3. **d,** Broadband transient absorption map recorded in transmission geometry ($-\Delta T/T$). Below the optical gap, the color scale was modified as indicated to highlight the spectrally broad photoinduced absorption (PIA) centered around 550 nm (pump wavelength 330 nm, pump energy 0.7 µJ, T = 77 K). **e,** Dynamics extracted at 425 nm (X_3), 445 nm (X_2), 456 nm (X_1), and 550 nm (PIA). The signal of X_1 (light blue dots) is delayed by about 500 fs with respect to X_2 and X_3 (blue and dark blue dots). The rise of the PIA (red) matches closely the decay of the excitonic features. The solid lines are smoothed to highlight the trend.

To disentangle the effect of free carriers vs. excitons in the trapping process, we turn to resonant excitation of the excitons (Figure 2, pump wavelength 425 nm, T = 77 K). We distinguish three distinct regimes (labelled I,II, and III). For t < 600 fs (regime I), the dynamics are governed by an initial relaxation of the non-equilibrium carrier population (Fig. 2b). While the photoinduced bleachings (minima in $-\Delta T/T$) of X_3 and X_2 decay, the photoinduced bleaching of X_1 rises (highlighted by the arrows in Fig. 2a and Fig. 2b), indicating relaxation and energy transfer into the lowest transition X_1. We resolve a further feature at 385 nm, which matches closely the step-like onset found in steady-state absorption (cf. Fig. 1b) and may correspond either to the onset of the continuum (significantly blue-shifted compared to room temperature) or a higher excitonic transition.

	X1	X2	X3
center	2.727 ± 0.003 eV (455 nm)	2.792 ± 0.002 eV (444 nm)	2.872 ± 0.002 eV (431 nm)
width	18 ± 0.3 meV (3.0 nm)	26 ± 0.2 meV (4.1 nm)	45 ± 0.3 meV (6.5 nm)
spectral weight	0.0066124	0.024	0.090

In addition to photoinduced bleaching, the response comprises also spectral shifts of the transitions, visible by the combined positive and negative transmission changes. For 2D excitons screening and band gap renormalization effects can play a dominant role in the ultrafast response,[31,32] and they have been shown to lead to shifts of the optical transitions. Tuning the excitation wavelength (Supplementary Fig. S2), we found that also the higher lying transitions (X_3 and X_2) shift even when pumping only the lowest transition X_1. Such a collective shift of all transitions, independent of the excitation, can be understood by bandgap renormalization and screening due to the photogenerated charge carriers, as has been shown for MoS_2, WSe_2, and other 2D materials.[31,33–35] This hypothesis is further corroborated by similar relaxation times of X_1, X_2 and X_3 for all pump wavelengths (Supplementary Fig. S3), suggesting a common origin. Generally, the interplay between the renormalizations of single particle gap and exciton binding energy can be complex in 2D systems.[1] For 2D transition metal dichalcogenides, they compensate to a large extent such that the overall shifts of the optical transitions can be rather small (on the order of 10 meV) while the change in single particle gap (or equivalently exciton binding energy) may be rather large (on the order of 100 meV).[36]

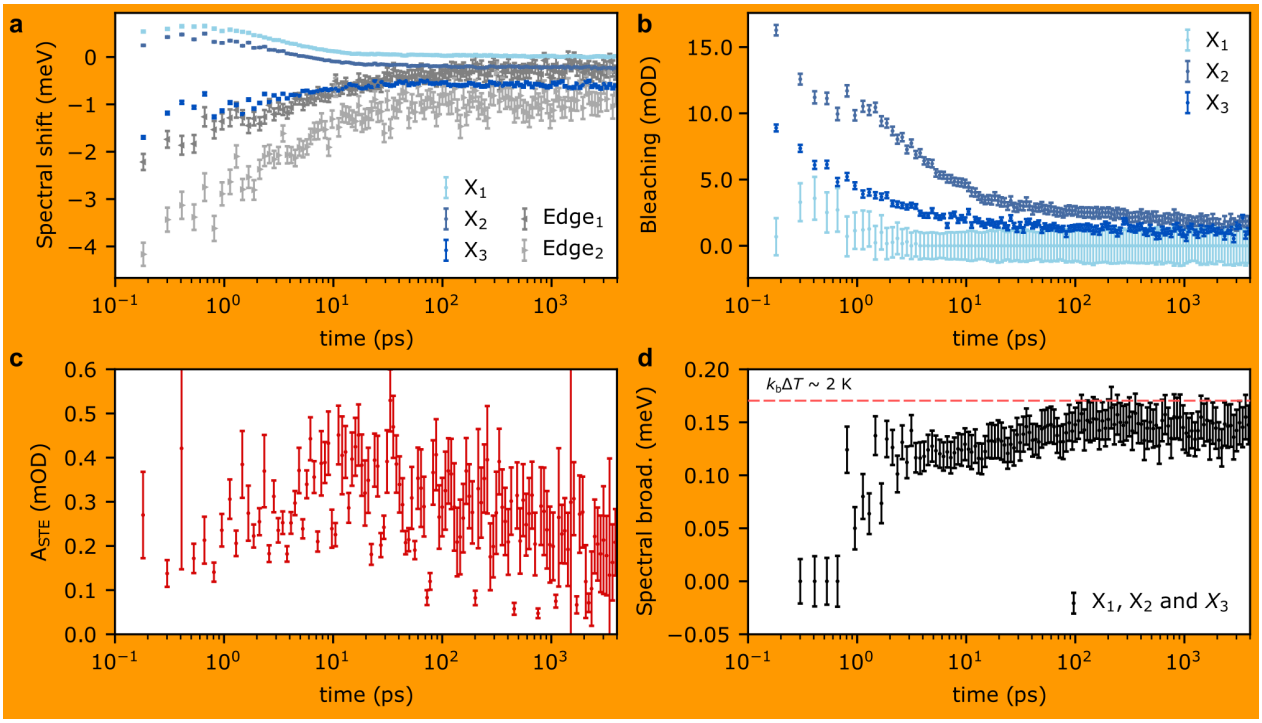

To better resolve the several effects involved we turned to lineshape analysis, deconvolving the transient absorption spectra based on steady state absorption modelling (Fig. 02). This procedure allows to disentangle peaks bleaching, broadening and shifting. Such variations correlated with ground transition blocking, temperature induced transition broadening and bandgap renormalization or screening, respectively. From our analysis the main TA effects on the short timescales result to be dominated by peak shift upon carriers excitations (for both excitons and free carriers). The peak shifts are different for X_1 and X_2 (blue-shift) compared to X_3 (red-shift). This is understood in terms of significant bandgap renormalization and concomitant exciton screening variation due to excited particles. The first causes the band edge along with the highest energy exciton to move to lower energy while the second reduces the exciton binding energy for the tightly bounded X_1, X_2. […] Our model successfully captures the main features of the TA spectra. In detail, the X1 bleaching due to population filling [...], and the rise of the thermal component (spectral broadening, see Supporting Figure XX) are resolved and match the experimentally observed data.

Since the intensity variation of the peaks are univocally associated with each exciton response we deconvolved in terms of shifting and bleaching, we carry out the following analysis considering the TA peak intensity as good indicators of the excitonic population. Therefore we turn in the analysis of excited state dynamics, by individuating 3 different time ranges where different physical phenomena dominates the TA signal.

From 0.6 ps < t < 10 ps (regime II, Fig. 2c), X_1, X_2, and X_3 decay with similar time constants, and the photoinduced absorption associated with trapping (PIA centered at 550 nm) arises, similar to the case of free carrier pumping (cf. Fig. 1d and Supplementary Fig. S4). For t > 10 ps (regime III, Fig. 2d), we find that the lineshape of the transient absorption signal, can be

described solely by temperature-induced changes of the steady-state absorbance spectrum ΔA = A(*T*) - A(*T*+Δ*T*), where *T* is the temperature and A the steady state absorbance (Supplementary Fig. S5). In other words, any additional, non-radiative relaxation pathways, including laser heating effects, have lead to a transiently heated phonon bath, which impacts the excitonic absorption (cf. Fig. 1b). On the basis of the experimentally measured temperature dependence of the steady state absorption, we can estimate the increase of the lattice temperature to be 0.9 K at *t* = 4 ns for a 0.04 µJ pulse (Supplementary Fig. S5), which is a common order of magnitude for lattice heating effects in thin films [Kastl2015 Nature Comm]. On the quartz substrates, the phonon temperature exhibits a slow nanosecond decay past the instrumental limit. Although the PIA band still persists as well for *t* > 10 ps, its decay time (XXX ± XX ps) is significantly shorter than the determined decay time of the phonon temperature (> 4 ns). Consistently, we also find no evidence of a temperature-dependent subgap absorption in the steady-state spectra which may mimic the photoinduced transition absorption. Therefore we exclude temperature effects to be the origin of the PIA band.

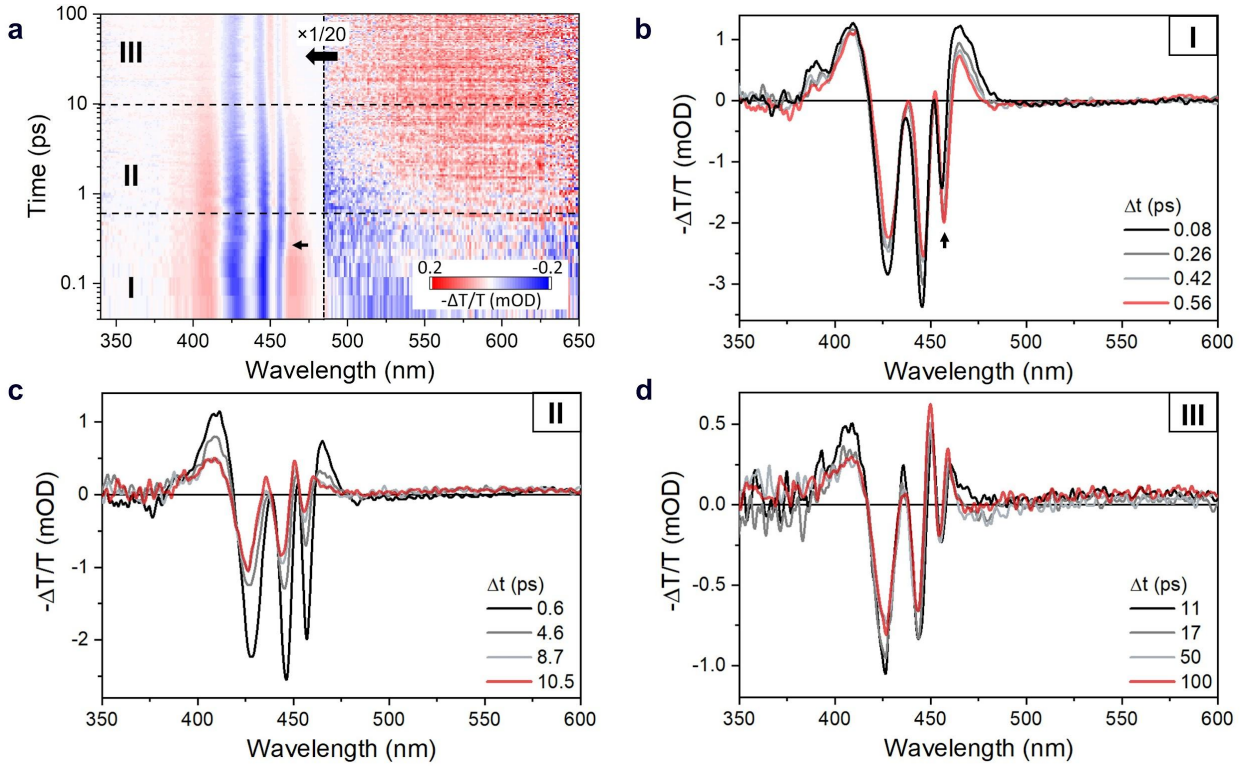

Figure 2. Transient absorption spectroscopy for excitonic pumping at 6 K. **a,** Broadband TA map in logarithmic representation. Three distinct temporal regimes can be discerned as indicated by dashed lines corresponding to thermalization and relaxation (I), exciton self-trapping (II), and phonon cooling to the substrate (III). For wavelength above 480 nm the color scale was adjusted as indicated. **b-d,** Transient absorption spectra for specific time delays in the different regimes (pump wavelength 425 nm, pump energy 0.015 µJ, *T* = 6 K).

Figure 3 depicts the pump fluence dependence, both for resonant excitonic pumping of X_3 (pump wavelength 429 nm, Fig. 3a-c) and free carrier pumping (pump wavelength 330 nm, Fig.

3d-f). Figure 3a shows the response at t = 150 fs normalized by the pump fluence. The spectra comprise clear bleaching of all three excitons (negative peaks in Fig. 3a). Figure 3b shows the fluence dependence evaluated at the position of the negative peaks. As expected, the transition X_3, which is the one being pumped directly, shows an almost linear behaviour (slope 0.94 ± 0.01), and it saturates only for the highest pump fluences > 0.2 µJ, equivalent to an exciton density per layer > $3 \cdot 10^{13}$ cm^{-2}. We estimated the latter from the steady-state absorbance and the film thickness. For the largest pump fluences, alongside possible Auger-assisted recombination,[37,38] slight degradation occurred, which may cause the sublinear trend.

Figure 3. Pulse fluence dependence of the TA for excitonic pumping(pump wavelength 429 nm) **(a-c)** and above bandgap pumping (pump wavelength 330 nm) **(d-e)** at T = 77 K. **a,d,** Instantaneous TA signal after the pump normalized by pump fluence. **b,e,** Maximum TA signal vs. pump fluence for the three excitonic features peaks and the photoinduced absorption band (PIA) in double logarithmic representation. The dashed lines are power law fits. The black dashed line indicates the slope of a power law with exponent p = 1. **c,f,** Time constants extracted from an exponential fit vs. pump fluence for X_1, X_2, X_3 and the PIA band. The top axis labels represent the effective exciton density per layer estimated from the steady state absorbance and film thickness.

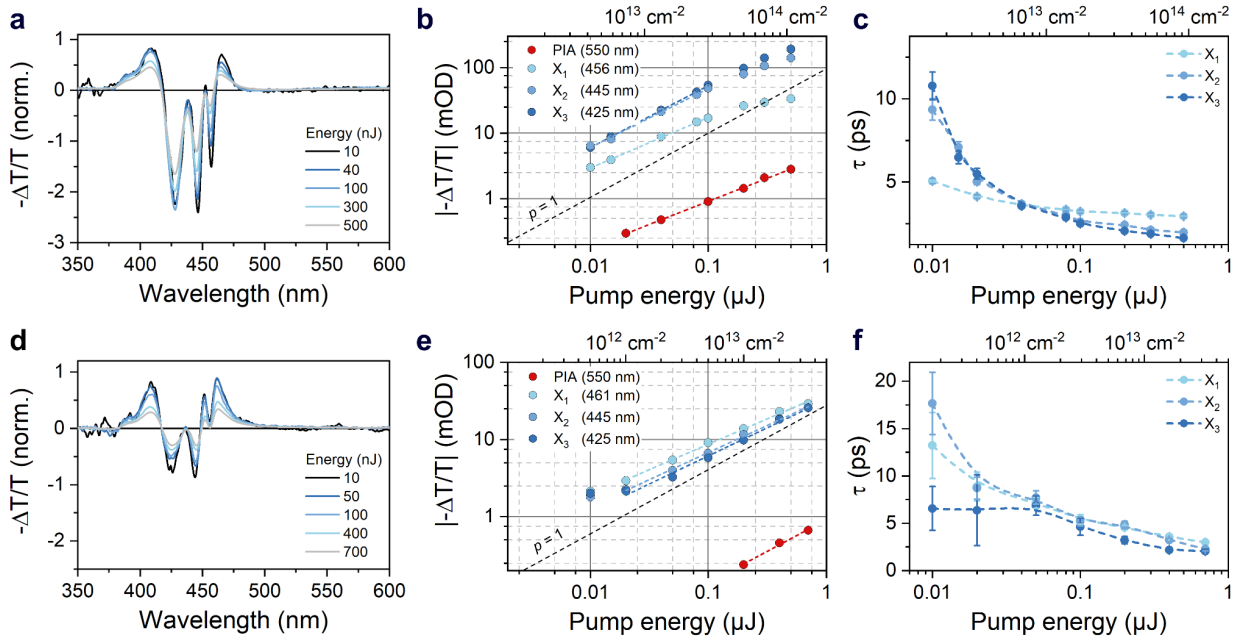

The lowest transition X_1 is markedly different with a sublinear dependence (0.77 ± 0.01) starting for the lowest pump energies of 0.01 µJ (corresponding to an exciton density per layer of $6 \cdot 10^{11}$ cm^{-2}). The PIA at 550 nm exhibits a similar sublinear dependence (slope 0.71 ± 0.02). The common slopes suggest that the 550 nm band is populated from X_1, in other words, that X_1 is trapped. The sublinearity of X_1 furthermore suggests that in addition to the fast population of X_1 via X_3 (~500 fs), another competing process can relax the higher excitonic states, which is likely

direct trapping of X_2 and X_3. A sublinear dependence of the trapped exciton is often attributed to a saturation of a finite number of trapping sites, suggesting extrinsic, defect-mediated trapping.[21,39] However in the present case, X_1 shows already a sublinear dependence, such that we cannot unambiguously assign the sublinear slope of PIA to a defect-mediated process. Furthermore, we find similar signatures of self-trapping in single crystals (Supplementary Fig. S6), which we expect to have lower defect density than the nanocrystalline films. Therefore, trapping of excitons is likely an intrinsic property of $[AgSePh]_\infty$.

In Fig. 3c, we plot the decay times extracted from an exponential fit. Although multiple level systems can generally exhibit non-exponential behavior,[40] the decay dynamics can be satisfactorily approximated by an exponential model (Supplementary Fig. S7 and Supplementary Fig. S8). The relaxation time of X_1 is 3 ps < τ_{X1} < 5 ps and it depends only weakly on excitation density. The fluence dependence of X_2 and X_3 suggests that τ_{X2}, τ_{X3} are impacted by a carrier density dependent mechanism, such as exciton-exciton interactions. For example, in the context of 2D transition metal dichalcogenides, experiments evidenced an excitonic Mott transition around 10^{13} cm^{-2},[41,42] and theoretical work suggests that, depending on the residual carrier density as well as the dielectric screening, free carriers and excitons coexist already substantially below the Mott transition.[43] Such presence of free carriers may explain features related to spectral shifts, such as the photoinduced absorption (positive peak) at 410 nm in Fig. 3a. Furthermore, in the presence of free carriers, Auger recombination is known to be an effective relaxation pathway, both for the excitons as well as the free carriers, and it may contribute to the observed density dependence of the dynamics of X_2 and X_3.[37,38]

Figures 3d-f depict free carrier pumping above the quasiparticle gap (pump wavelength 330 nm). Notably, the spectra in Fig. 3d comprise mainly shift signals, i.e. the response across the oscillators averages to zero. These shifts can be understood by a dominating effect of band gap renormalization due to screening from the free carriers. In a simplistic model, screening due to free carriers is twice as large compared to bound excitons.[33,44] Such screening should impact all transitions alike, consistent with the common power law (Fig. 3e) and decay time (Fig. 3f) for X_1, X_2 and X_3 within the experimental uncertainty.[31] Importantly, the PIA is reduced approximately by a factor of 2 (red dots in Fig. 3b, Fig. 3e and Supplementary Fig. S9) compared to resonant pumping (at the equal density of optically generated electron-hole pairs), suggesting direct trapping of excitons rather than trapping of free carriers as the dominant mechanism. The overall timescales and spectral responses are independently corroborated by a global analysis of the data (Supplementary Fig. S10).

Finally, we discuss the temperature dependence of the carrier dynamics. Overall, the dynamics are only weakly temperature dependent, but show a systematic non-monotonous behavior (Fig. 4a and Supplementary Fig. S11). The dynamics accelerate slightly as the temperature is decreased, and for temperatures below 50 K, the exciton lifetime appears to increase again. The rise time of the STE, as extracted from the maximum of the PIA, mimics the temperature dependence of the exciton decay, underscoring the connection between exciton decay and filling of the trapped states. The decrease of lifetime with decreasing temperature suggests that phonon scattering is not the limiting factor. Phonon-assisted, non-radiative recombination would generally show the opposite trend, with longer lifetimes at lower temperatures.[45] A combination

of exciton self-trapping and dynamic detrapping can explain the non-monotonic temperature dependence. Without considering the microscopic details, a general coordinate representation can describe the trapping process (Fig. 4b). To reach the self-trapped state, the exciton has to overcome an energy barrier, e.g. a lattice deformation at the localization site.[46] The corresponding energy barrier for the inverse process (detrapping) is typically larger, because the final trapped state, after intermediate relaxation, has an overall lower energy configuration (Fig. 4b).[46] With decreasing temperature, the detrapping probability decreases faster than the trapping probability, leading to an overall higher trapping rate. In our interpretation, when the temperature falls below 50 K, the trapping process becomes the slowest, rate limiting step, and the exciton lifetime increases again.[46] A similar, non-monotonic behavior was observed in photoluminescence spectroscopy of $[AgSePh]_\infty$, without considering the impact of self-trapping.[20] As depicted in Fig. 4b, radiative recombination from the self-trapped excited state to the ground state, which is displaced from the free exciton configuration, can occur via a continuum of allowed transitions, consistent with the broad sub-gap photoluminescence at low-temperatures (Supplementary Figure S1).

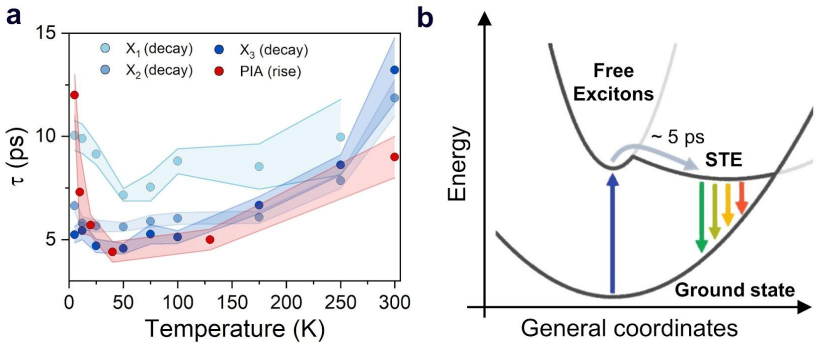

Figure 4. a, Temperature dependence of exciton dynamics. The exciton decays are weakly temperature dependent, but follow closely the trapping dynamics. Below 50 K, the thermal energy is not sufficient for promoting the exciton trapping process above the activation energy, causing an increase of exciton lifetime. The shaded areas denote the uncertainty of the parameters (pump wavelength 330 nm, pump energy 0.02 µJ). **b,** Schematic general coordinate diagram of the excitonic transitions, the trapping barrier, and the final self-trapped exciton state. The blue arrow denotes the optical excitation of free excitons. The colored arrows indicate possible radiative recombination pathways of the trapped state.

Conclusions

For the hybrid quantum well material $[AgSePh]_\infty$, we found transient signatures of three excitonic transitions X_1, X_2 and X_3, which are also present in steady-state absorption, as well as a broad photoinduced absorption below the optical gap, which is only present after optical excitation. The transient excitonic features can be assigned to a combination of bandgap renormalization and ground state depletion induced by excited carriers . For pumping of free carriers above the optical gap, we determined the formation time of the lowest lying exciton X_1 to be on the order of 500 fs. As a main finding, we identified the sub-gap, photoinduced

absorption as the signature of self-trapped excitons. The self-trapped state is more efficiently populated by direct pumping of excitons compared to pumping of free carriers, indicating direct, intrinsic trapping as the microscopic mechanism. At cryogenic temperatures, the trapped excitons are likely the origin of broadband sub-gap emission, observed also previously.[4,20] For temperatures below 50 K, we found a decrease of the self-trapped exciton population, which we assign to a lower probability of thermal activation across the energy barrier associated with the trapping process. Overall, the trapping is fast and depopulates the excited carriers within a few picoseconds. $[AgSePh]_\infty$ may find application as an optical ultrafast switch, and self-trapping could be used in general as a driving concept for achieving ultrafast, charge neutral de-excitation in similar material systems.

SUPPORTING INFORMATION

The SI are available online.

METHODS

Synthesis of $[AgSePh]_\infty$ (silver benzeneselenolate). The films were synthesized according to a protocol previously described in Ref. [4]. Briefly, 10 nm thin films of silver were thermally evaporated on fused silica substrates. Subsequently, the Ag films were exposed to UV ozone for 10 min to oxidize silver. The oxidized silver films were reacted with benzeneselenol (PhSeH) by vapour transport for 2 hours in an oven at 80 °C.The samples were rinsed in IPA to remove the unreacted benzeneselenol and N_2 dried.

Steady state absorption spectroscopy. Temperature dependent absorption spectra were obtained by measuring transmission spectra on a commercial PerkinElmer Lambda 1050 UV/Vis/NIR spectrometer. The samples were mounted in a nitrogen flow cryostat (Linkam THMS350V).

Photoluminescence spectroscopy. Low temperature photoluminescence was collected by a confocal microscope (inVia Raman Microscope Renishaw) using a 20X objective and an excitation wavelength of 442 nm. The samples were mounted in a nitrogen flow cryostat (Linkam THMS350V).

Transient absorption spectroscopy. We used an ultrafast transient absorption system with a tuneable pump and white-light probe to measure the differential transmission through thin benzene silverselenolate films supported on quartz substrates. The laser system consists of a regeneratively amplified Ti:sapphire oscillator (Coherent Libra), which delivers 4 mJ pulse energies centred at 800 nm with a 1 kHz repetition rate. The pulse duration of the amplified pulse is approximately 80 fs. The laser output was split by an optical wedge to produce the pump and probe beams and the pump beam wavelength was tuned by an optical parametric amplifier (Coherent OPerA). The pump beam was focused onto the sample by spherical lens at near-normal incidence (spot size FWHM ~ 300 μm). The probe beam was focused onto a sapphire plate to generate a white-light continuum probe, which was collected and refocused onto the sample by a spherical mirror (spot size FWHM ~ 150 μm). The transmitted whitelight

was collected and analysed with a commercial absorption spectrometer (Helios, Ultrafast Systems LLC). Pulse-to-pulse fluctuations of the whitelight continuum were accounted for by a simultaneous reference measurement of the continuum. Pump and probe beam were linearly cross-polarized and any scattered pump-light into the detection path was filtered by a linear polarizer. The time delay was adjusted by delaying the pump pulse with a linear translation stage (minimum step size 16 fs). The sample was mounted directly on the cold finger of a He-flow cryostat (Janis ST-500) by silver paste. The temperature was measured at the cold finger. All measurements were conducted in vacuum ($p \sim 10^{-5}$ mbar).

AUTHOR INFORMATION

The authors declare no competing financial interests.

ACKNOWLEDGMENT

Work at the Molecular Foundry was supported by the Center for Novel Pathways to Quantum Coherence in Materials, Office of Science, Office of Basic Energy Sciences, of the U.S. Department of Energy under contract no. DE-AC02-05CH11231. L.M. thanks D. Cortecchia for helping with low-temperature steady state absorption measurements.

AUTHOR CONTRIBUTIONS

C.K., A.M.S., and L.M. conceived and designed the experiments. L.M. synthesized the material. C.K. and L.M. performed transient absorption spectroscopy at the Molecular Foundry. L.M. performed optical spectroscopy at IIT. C.K. and L.M. analyzed the experimental data and wrote the manuscript with input from all authors. All authors reviewed the manuscript.

REFERENCES

(1) Wang, G.; Chernikov, A.; Glazov, M. M.; Heinz, T. F.; Marie, X.; Amand, T.; Urbaszek, B. Colloquium: Excitons in Atomically Thin Transition Metal Dichalcogenides. *Rev. Mod. Phys.* **2018**, *90* (2), 021001. https://doi.org/10.1103/RevModPhys.90.021001.

(2) Chen, Y.; Sun, Y.; Peng, J.; Tang, J.; Zheng, K.; Liang, Z. 2D Ruddlesden–Popper Perovskites for Optoelectronics. *Adv. Mater.* **2018**, *30* (2), 1703487. https://doi.org/10.1002/adma.201703487.

(3) Blancon, J.-C.; Even, J.; Stoumpos, Costas. C.; Kanatzidis, Mercouri. G.; Mohite, A. D. Semiconductor Physics of Organic–Inorganic 2D Halide Perovskites. *Nat. Nanotechnol.* **2020**, *15* (12), 969–985. https://doi.org/10.1038/s41565-020-00811-1.

(4) Maserati, L.; Refaely-Abramson, S.; Kastl, C.; Chen, C. T.; Borys, N. J.; Eisler, C. N.; Collins, M. S.; Smidt, T. E.; Barnard, E. S.; Strasbourg, M.; Schriber, E. A.; Shevitski, B.; Yao, K.; Hohman, J. N.; Schuck, P. J.; Aloni, S.; Neaton, J. B.; Schwartzberg, A. M. Anisotropic 2D Excitons Unveiled in Organic–Inorganic Quantum Wells. *Mater. Horiz.* **2021**, *8* (1), 197–208. https://doi.org/10.1039/C9MH01917K.

(5) Miller, D. A. B. *Optical Physics of Quantum Wells*; 1996.

(6) Milichko, V. A.; Makarov, S. V.; Yulin, A. V.; Vinogradov, A. V.; Krasilin, A. A.; Ushakova, E.; Dzyuba, V. P.; Hey-Hawkins, E.; Pidko, E. A.; Belov, P. A. Van Der Waals Metal-Organic Framework as an Excitonic Material for Advanced Photonics. *Adv. Mater.* **2017**, *29* (12), 1606034. https://doi.org/10.1002/adma.201606034.
(7) Li, Y.; Jiang, X.; Fu, Z.; Huang, Q.; Wang, G.-E.; Deng, W.-H.; Wang, C.; Li, Z.; Yin, W.; Chen, B.; Xu, G. Coordination Assembly of 2D Ordered Organic Metal Chalcogenides with Widely Tunable Electronic Band Gaps. *Nat. Commun.* **2020**, *11* (1), 261. https://doi.org/10.1038/s41467-019-14136-8.
(8) Tran, M.; Kline, K.; Qin, Y.; Shen, Y.; Green, M. D.; Tongay, S. 2D Coordination Polymers: Design Guidelines and Materials Perspective. *Appl. Phys. Rev.* **2019**, *6* (4), 041311. https://doi.org/10.1063/1.5110895.
(9) Maserati, L.; Prato, M.; Pecorario, S.; Passarella, B.; Perinot, A.; Thomas, A. A.; Melloni, F.; Natali, D.; Caironi, M. Photo-Electrical Properties of 2D Quantum Confined Metal–Organic Chalcogenide Nanocrystal Films. *Nanoscale* **2021**, *13* (1), 233–241. https://doi.org/10.1039/D0NR07409H.
(10) Peach, M. E. Preparation and Thermal Decomposition of Some Metal Thiophenolates. *J. Inorg. Nucl. Chem.* **1979**, *41* (9), 1390–1392. https://doi.org/10.1016/0022-1902(79)80062-7.
(11) Veselska, O.; Demessence, A. D10 Coinage Metal Organic Chalcogenolates: From Oligomers to Coordination Polymers. *Divers. Coord. Chem. Spec. Issue Honor Prof Pierre Braunstein - Part II* **2018**, *355*, 240–270. https://doi.org/10.1016/j.ccr.2017.08.014.
(12) Smith, S. C.; Bryks, W.; Tao, A. R. Supramolecular Assembly of Single-Source Metal–Chalcogenide Nanocrystal Precursors. *Langmuir* **2019**, *35* (8), 2887–2897. https://doi.org/10.1021/acs.langmuir.8b01043.
(13) Huang, X.; Li, J.; Fu, H. The First Covalent Organic−Inorganic Networks of Hybrid Chalcogenides: Structures That May Lead to a New Type of Quantum Wells. *J. Am. Chem. Soc.* **2000**, *122* (36), 8789–8790. https://doi.org/10.1021/ja002224n.
(14) Eichhöfer, A.; Buth, G.; Dolci, F.; Fink, K.; Mole, Richard. A.; Wood, P. T. Homoleptic 1-D Iron Selenolate Complexes—Synthesis, Structure, Magnetic and Thermal Behaviour of $_{\infty}^{1}$[Fe(SeR)$_2$] (R = Ph, Mes). *Dalton Trans.* **2011**, *40* (26), 7022–7032. https://doi.org/10.1039/C1DT10089K.
(15) Eichhöfer, A.; Lebedkin, S. 1D and 3D Polymeric Manganese(II) Thiolato Complexes: Synthesis, Structure, and Properties of $_{\infty}^{3}$[Mn$_4$(SPh)$_8$] and $_{\infty}^{1}$[Mn(SMes)$_2$]. *Inorg. Chem.* **2018**, *57* (2), 602–608. https://doi.org/10.1021/acs.inorgchem.7b02411.
(16) Eichhöfer, A.; Buth, G. 1-D Polymeric Iron(II) Thiolato Complexes: Synthesis, Structure, and Properties of $_{\infty}^{1}$[Fe(SR)$_2$] (R = Ph, Mes), $_{\infty}^{1}$[Fe(NH$_3$)(SPh)(μ-SPh)] and $_{\infty}^{1}$[(μ-SPh)Fe(NH$_3$)$_2$(μ-SPh)$_2$Fe(μ-SPh)]. *Eur. J. Inorg. Chem.* **2019**, *2019* (5), 639–646. https://doi.org/10.1002/ejic.201801178.
(17) Lavenn, C.; Okhrimenko, L.; Guillou, N.; Monge, M.; Ledoux, G.; Dujardin, C.; Chiriac, R.; Fateeva, A.; Demessence, A. A Luminescent Double Helical Gold(i)–Thiophenolate Coordination Polymer Obtained by Hydrothermal Synthesis or by Thermal Solid-State Amorphous-to-Crystalline Isomerization. *J. Mater. Chem. C* **2015**, *3* (16), 4115–4125. https://doi.org/10.1039/C5TC00119F.
(18) Liu, W.; Lustig, W. P.; Li, J. Luminescent Inorganic-Organic Hybrid Semiconductor Materials for Energy-Saving Lighting Applications. *EnergyChem* **2019**, *1* (2), 100008. https://doi.org/10.1016/j.enchem.2019.100008.
(19) Cuthbert, H. L.; Wallbank, A. I.; Taylor, N. J.; Corrigan, J. F. Synthesis and Structural Characterization of [Cu20Se4(M3-SePh)12(PPh3)6] and [Ag(SePh)]∞. *Z. Für Anorg. Allg. Chem.* **2002**, *628* (11), 2483–2488. https://doi.org/10.1002/1521-3749(200211)628:11<2483::AID-ZAAC2483>3.0.CO;2-U.
(20) Yao, K.; Collins, M. S.; Nell, K. M.; Barnard, E. S.; Borys, N. J.; Kuykendall, T.; Hohman,

J. N.; Schuck, P. J. Strongly Quantum-Confined Blue-Emitting Excitons in Chemically Configurable Multiquantum Wells. *ACS Nano* **2020**. https://doi.org/10.1021/acsnano.0c08096.
(21) Yang, Z.; Wang, X.; Chen, Y.; Zheng, Z.; Chen, Z.; Xu, W.; Liu, W.; Yang, Y. (Michael); Zhao, J.; Chen, T.; Zhu, H. Ultrafast Self-Trapping of Photoexcited Carriers Sets the Upper Limit on Antimony Trisulfide Photovoltaic Devices. *Nat. Commun.* **2019**, *10* (1), 4540. https://doi.org/10.1038/s41467-019-12445-6.
(22) Grinblat, G.; Abdelwahab, I.; Nielsen, M. P.; Dichtl, P.; Leng, K.; Oulton, R. F.; Loh, K. P.; Maier, S. A. Ultrafast All-Optical Modulation in 2D Hybrid Perovskites. *ACS Nano* **2019**, *13* (8), 9504–9510. https://doi.org/10.1021/acsnano.9b04483.
(23) Li, S.; Luo, J.; Liu, J.; Tang, J. Self-Trapped Excitons in All-Inorganic Halide Perovskites: Fundamentals, Status, and Potential Applications. *J. Phys. Chem. Lett.* **2019**, *10* (8), 1999–2007. https://doi.org/10.1021/acs.jpclett.8b03604.
(24) Maserati, L.; Pecorario, S.; Prato, M.; Caironi, M. Understanding the Synthetic Pathway to Large-Area, High-Quality [AgSePh]∞ Nanocrystal Films. *J. Phys. Chem. C* **2020**, *124* (41), 22845–22852. https://doi.org/10.1021/acs.jpcc.0c07330.
(25) Cooper, J. K.; Reyes-Lillo, S. E.; Hess, L. H.; Jiang, C.-M.; Neaton, J. B.; Sharp, I. D. Physical Origins of the Transient Absorption Spectra and Dynamics in Thin-Film Semiconductors: The Case of BiVO4. *J. Phys. Chem. C* **2018**, *122* (36), 20642–20652. https://doi.org/10.1021/acs.jpcc.8b06645.
(26) Smith, M. D.; Karunadasa, H. I. White-Light Emission from Layered Halide Perovskites. *Acc. Chem. Res.* **2018**, *51* (3), 619–627. https://doi.org/10.1021/acs.accounts.7b00433.
(27) Li, J.; Wang, H.; Li, D. Self-Trapped Excitons in Two-Dimensional Perovskites. *Front. Optoelectron.* **2020**, *13* (3), 225–234. https://doi.org/10.1007/s12200-020-1051-x.
(28) Williams, R. T.; Song, K. S. The Self-Trapped Exciton. *J. Phys. Chem. Solids* **1990**, *51* (7), 679–716. https://doi.org/10.1016/0022-3697(90)90144-5.
(29) Itoh, N.; Stoneham, A. M.; Harker, A. H. The Initial Protection of Defects in Alkali Halides: F and H Centre Production by Non-Radiative Decay of the Self-Trapped Exciton. *J. Phys. C Solid State Phys.* **1977**, *10* (21), 4197–4209. https://doi.org/10.1088/0022-3719/10/21/010.
(30) Richter, S.; Jia, F.; Heinrich, M.; Döring, S.; Peschel, U.; Tünnermann, A.; Nolte, S. The Role of Self-Trapped Excitons and Defects in the Formation of Nanogratings in Fused Silica. *Opt. Lett.* **2012**, *37* (4), 482–484. https://doi.org/10.1364/OL.37.000482.
(31) Pogna, E. A. A.; Marsili, M.; De Fazio, D.; Dal Conte, S.; Manzoni, C.; Sangalli, D.; Yoon, D.; Lombardo, A.; Ferrari, A. C.; Marini, A.; Cerullo, G.; Prezzi, D. Photo-Induced Bandgap Renormalization Governs the Ultrafast Response of Single-Layer MoS_2. *ACS Nano* **2016**, *10* (1), 1182–1188. https://doi.org/10.1021/acsnano.5b06488.
(32) Trovatello, C.; Katsch, F.; Borys, N. J.; Selig, M.; Yao, K.; Borrego-Varillas, R.; Scotognella, F.; Kriegel, I.; Yan, A.; Zettl, A.; Schuck, P. J.; Knorr, A.; Cerullo, G.; Conte, S. D. The Ultrafast Onset of Exciton Formation in 2D Semiconductors. *Nat. Commun.* **2020**, *11* (1), 5277. https://doi.org/10.1038/s41467-020-18835-5.
(33) Cunningham, P. D.; Hanbicki, A. T.; McCreary, K. M.; Jonker, B. T. Photoinduced Bandgap Renormalization and Exciton Binding Energy Reduction in WS2. *ACS Nano* **2017**, *11* (12), 12601–12608. https://doi.org/10.1021/acsnano.7b06885.
(34) Chen, Z.; Dong, J.; Papalazarou, E.; Marsi, M.; Giorgetti, C.; Zhang, Z.; Tian, B.; Rueff, J.-P.; Taleb-Ibrahimi, A.; Perfetti, L. Band Gap Renormalization, Carrier Multiplication, and Stark Broadening in Photoexcited Black Phosphorus. *Nano Lett.* **2019**, *19* (1), 488–493. https://doi.org/10.1021/acs.nanolett.8b04344.
(35) Price, M. B.; Butkus, J.; Jellicoe, T. C.; Sadhanala, A.; Briane, A.; Halpert, J. E.; Broch, K.; Hodgkiss, J. M.; Friend, R. H.; Deschler, F. Hot-Carrier Cooling and Photoinduced Refractive Index Changes in Organic–Inorganic Lead Halide Perovskites. *Nat. Commun.*

2015, *6* (1), 8420. https://doi.org/10.1038/ncomms9420.
(36) Yao, K.; Yan, A.; Kahn, S.; Suslu, A.; Liang, Y.; Barnard, E. S.; Tongay, S.; Zettl, A.; Borys, N. J.; Schuck, P. J. Optically Discriminating Carrier-Induced Quasiparticle Band Gap and Exciton Energy Renormalization in Monolayer MoS2. *Phys. Rev. Lett.* **2017**, *119* (8), 087401. https://doi.org/10.1103/PhysRevLett.119.087401.
(37) Landsberg, P. T. *Recombination in Semiconductors*; Cambridge University Press: Cambridge, 1992. https://doi.org/10.1017/CBO9780511470769.
(38) Jiang, Y.; Cui, M.; Li, S.; Sun, C.; Huang, Y.; Wei, J.; Zhang, L.; Lv, M.; Qin, C.; Liu, Y.; Yuan, M. Reducing the Impact of Auger Recombination in Quasi-2D Perovskite Light-Emitting Diodes. *Nat. Commun.* **2021**, *12* (1), 336. https://doi.org/10.1038/s41467-020-20555-9.
(39) Seo, M.; Yamaguchi, H.; Mohite, A. D.; Boubanga-Tombet, S.; Blancon, J.-C.; Najmaei, S.; Ajayan, P. M.; Lou, J.; Taylor, A. J.; Prasankumar, R. P. Ultrafast Optical Microscopy of Single Monolayer Molybdenum Disulfide Flakes. *Sci. Rep.* **2016**, *6* (1), 21601. https://doi.org/10.1038/srep21601.
(40) Senty, T. R.; Cushing, S. K.; Wang, C.; Matranga, C.; Bristow, A. D. Inverting Transient Absorption Data to Determine Transfer Rates in Quantum Dot–TiO2 Heterostructures. *J. Phys. Chem. C* **2015**, *119* (11), 6337–6343. https://doi.org/10.1021/jp512500g.
(41) Chernikov, A.; Ruppert, C.; Hill, H. M.; Rigosi, A. F.; Heinz, T. F. Population Inversion and Giant Bandgap Renormalization in Atomically Thin WS2 Layers. *Nat. Photonics* **2015**, *9* (7), 466–470. https://doi.org/10.1038/nphoton.2015.104.
(42) Dendzik, M.; Xian, R. P.; Perfetto, E.; Sangalli, D.; Kutnyakhov, D.; Dong, S.; Beaulieu, S.; Pincelli, T.; Pressacco, F.; Curcio, D.; Agustsson, S. Y.; Heber, M.; Hauer, J.; Wurth, W.; Brenner, G.; Acremann, Y.; Hofmann, P.; Wolf, M.; Marini, A.; Stefanucci, G.; Rettig, L.; Ernstorfer, R. Observation of an Excitonic Mott Transition through Ultrafast Core-Cum-Conduction Photoemission Spectroscopy. *Phys. Rev. Lett.* **2020**, *125* (9), 096401. https://doi.org/10.1103/PhysRevLett.125.096401.
(43) Steinhoff, A.; Florian, M.; Rösner, M.; Schönhoff, G.; Wehling, T. O.; Jahnke, F. Exciton Fission in Monolayer Transition Metal Dichalcogenide Semiconductors. *Nat. Commun.* **2017**, *8* (1), 1166. https://doi.org/10.1038/s41467-017-01298-6.
(44) Ceballos, F.; Cui, Q.; Bellus, M. Z.; Zhao, H. Exciton Formation in Monolayer Transition Metal Dichalcogenides. *Nanoscale* **2016**, *8* (22), 11681–11688. https://doi.org/10.1039/C6NR02516A.
(45) Guo, Z.; Wu, X.; Zhu, T.; Zhu, X.; Huang, L. Electron–Phonon Scattering in Atomically Thin 2D Perovskites. *ACS Nano* **2016**, *10* (11), 9992–9998. https://doi.org/10.1021/acsnano.6b04265.
(46) Paritmongkol, W.; Powers, E. R.; Dahod, N. S.; Tisdale, W. A. Two Origins of Broadband Emission in Multilayered 2D Lead Iodide Perovskites. *J. Phys. Chem. Lett.* **2020**, *11* (20), 8565–8572. https://doi.org/10.1021/acs.jpclett.0c02214.

Supporting Information

Exciton self-trapping causes picoseconds recombination in metal-organic chalcogenides quantum wells

Christoph Kastl[†§], Adam M. Schwartzberg[†], and Lorenzo Maserati[†‡]

† The Molecular Foundry, Lawrence Berkeley National Laboratory, Berkeley, California 94720, USA.

§ Walter Schottky Institute and Physik Department, Technical University of Munich, Garching 85748, Germany.

‡ Center for Nano Science and Technology @PoliMi, Istituto Italiano di Tecnologia, 20133 Milan, Italy.

Correspondence to: christoph.kastl@wsi.tum.de, amschwartzberg@lbl.gov, lmaserati@lbl.gov.

Table of contents

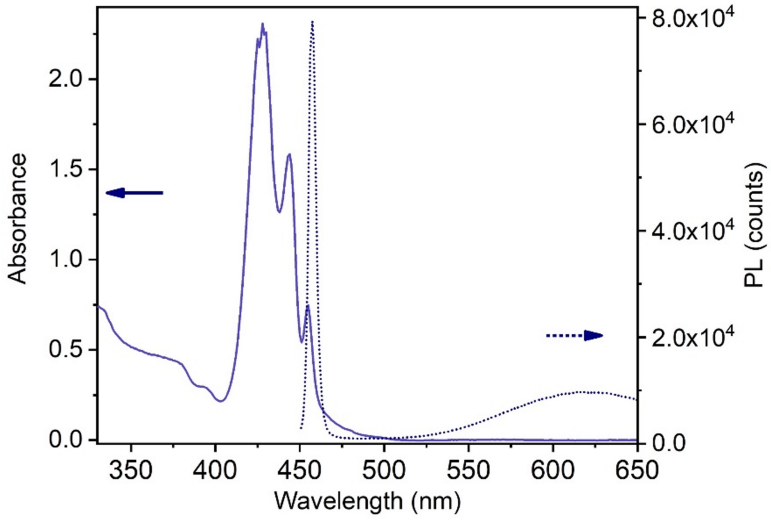

Figure S1. Absorbance and photo-luminescence (PL) spectra of $[AgSePh]_\infty$ film at 77 K.The absorption at 429 nm is about 1.22 times stronger than absorption at 330 nm. The PL comprises a narrow blue emission, corresponding to X_1 (with a Stokes shift of 14 meV), and a broad feature, indicative of trapped state emission, past 600 nm. The latter is not present in the steady state absorption spectrum.

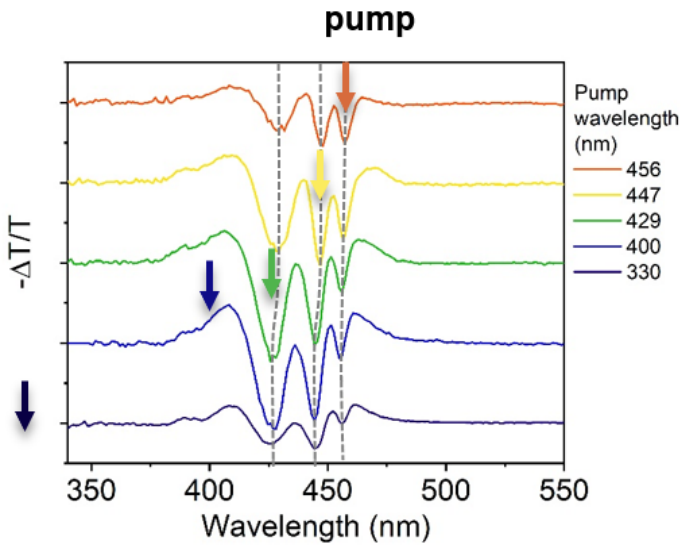

Figure S2. The overall shape of the transient absorption spectra directly after the pump pulse (*t* ~ 200 fs) depends only weakly on pump wavelength (indicated by the arrows). In particular, even for pumping only the lowest energy transition (X_1, pump wavelength 456 nm), a collective response of all excitons is observed. The latter can be understood by renormalization effects. *T* = 77 K.

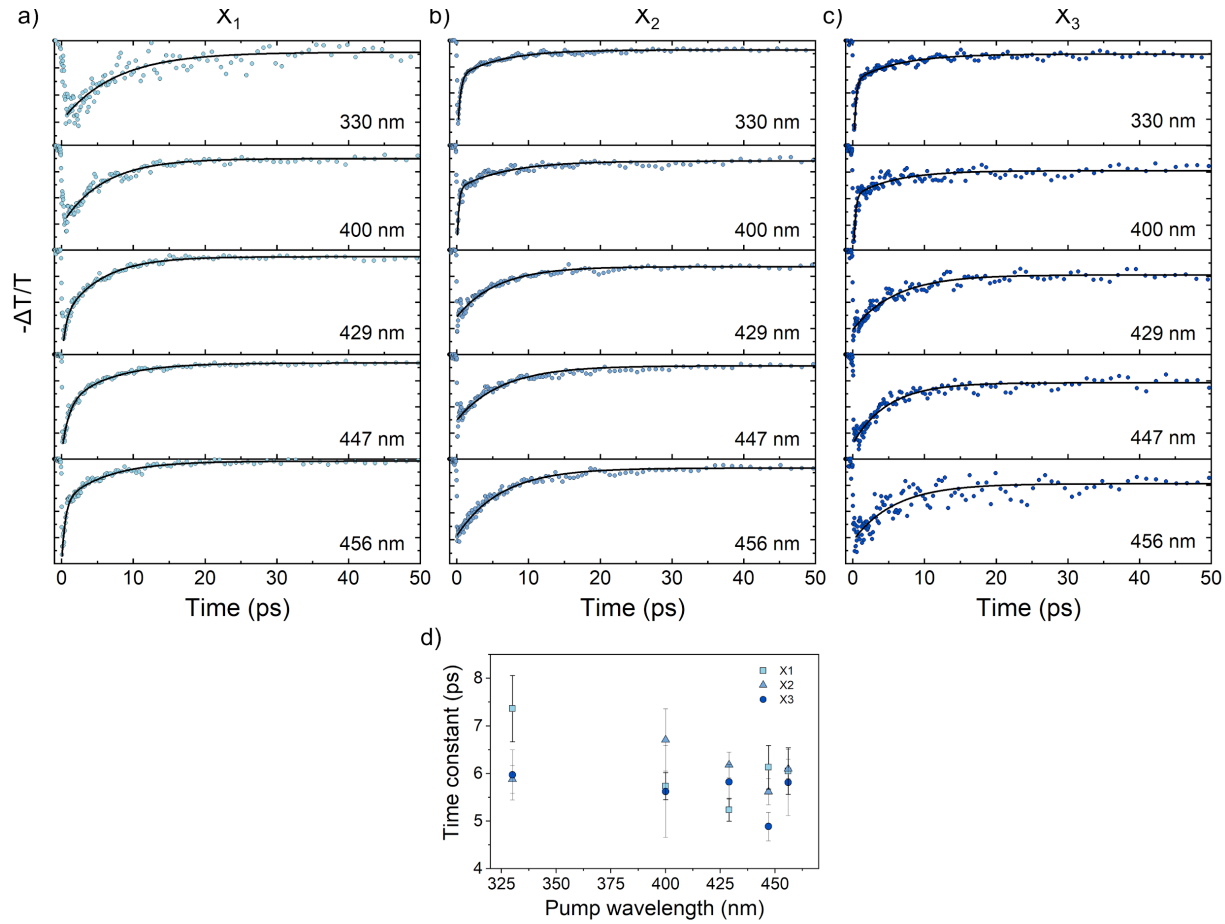

Figure S3. Exciton dynamics at different pump wavelengths. Dynamics of ΔT/T at fixed wavelengths corresponding to the three excitonic transitions. Data are depicted by dots and exponential fits are depicted by solid lines: **a**, X_1, 427 nm. **b,** X_2, 447 nm. **c,** X_3, 456 nm. All experiments were performed at 77 K and 0.02 µJ pulse energy. d) Summary of exponential decay time constants at different pump wavelengths. The fast (sub-ps) components which are related to hot carrier thermalization are omitted.

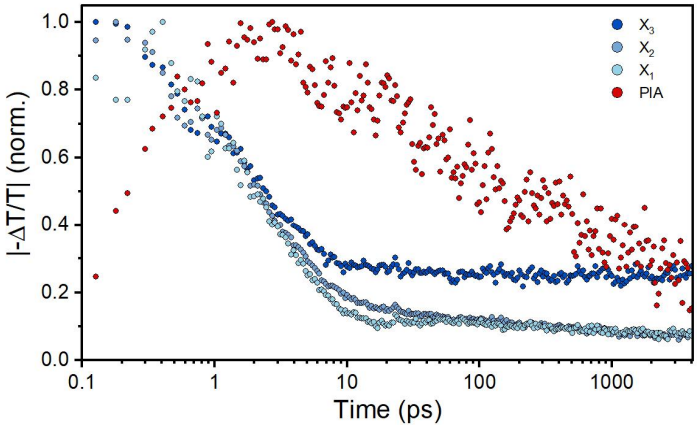

Figure S4. Dynamics extracted at the position of the excitonic transitions X_1, X_2, X_3 as well as at the photoinduced absorption band for direct excitonic pumping (pump wavelength 330 nm, pump energy 0.2 µJ, T = 77 K).

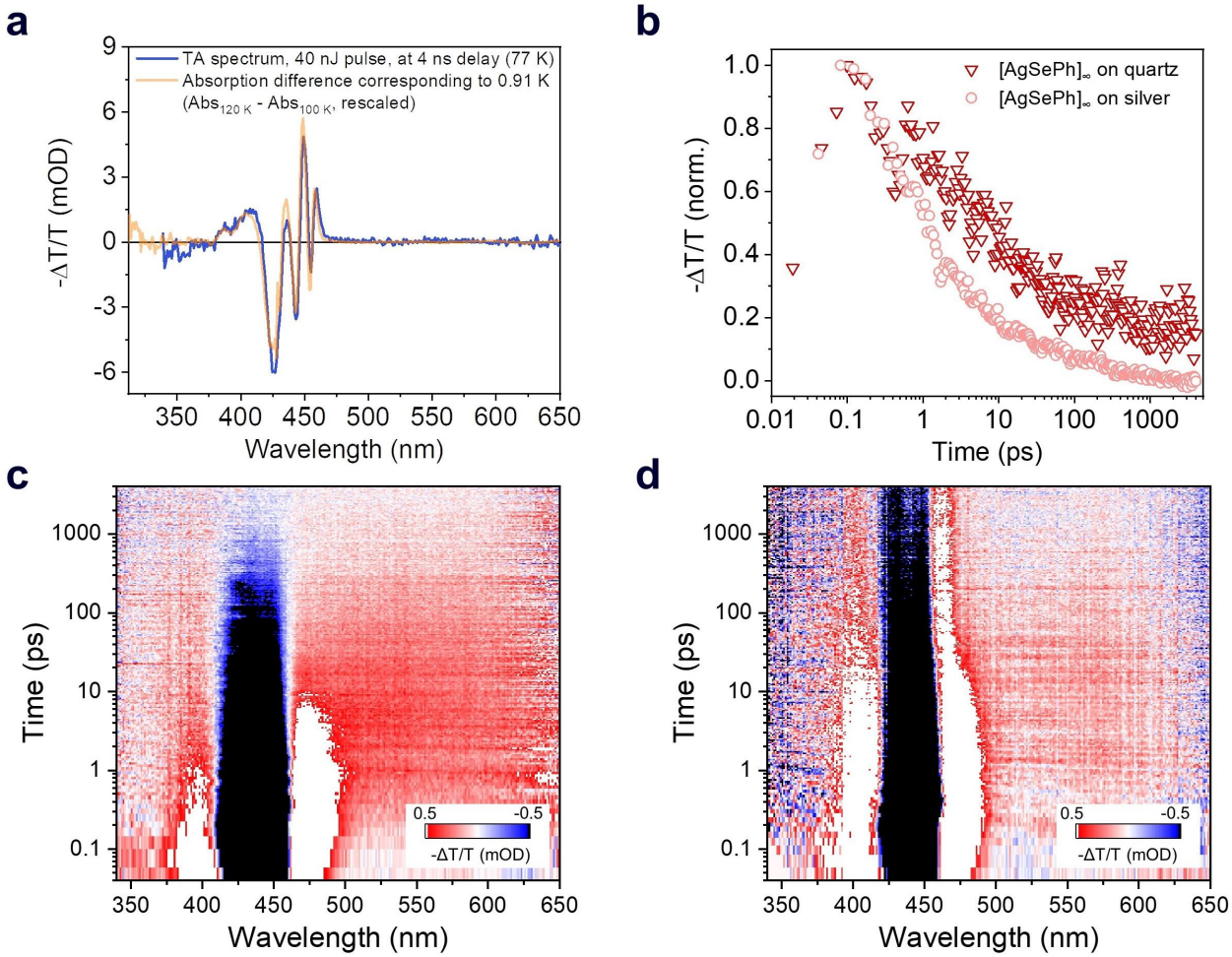

Figure S5. Heated phonon bath and cooling to substrate. **a,** At long time scales (~ns), the transient absorption spectrum (blue) is very well described by temperature induced changes of the steady state absorption spectrum (orange) **b,** Transient absorption dynamics extracted at the position of the excitonic transitions X_3, for thermally insulating substrate, i.e. quartz (dark red triangles) and thermally conducting substrate, i.e. silver film (light red circles). The thermal response persists longer (~ns) on a thermally insulating substrate compared to a thermally conductive one (~ 100 ps). **c,d** Room temperature transient absorption spectra of $[AgSePh]_\infty$ films, on silver **(c)** and quartz **(d)** substrates, respectively, pump wavelength 430 nm, pump energy 0.02 µJ.

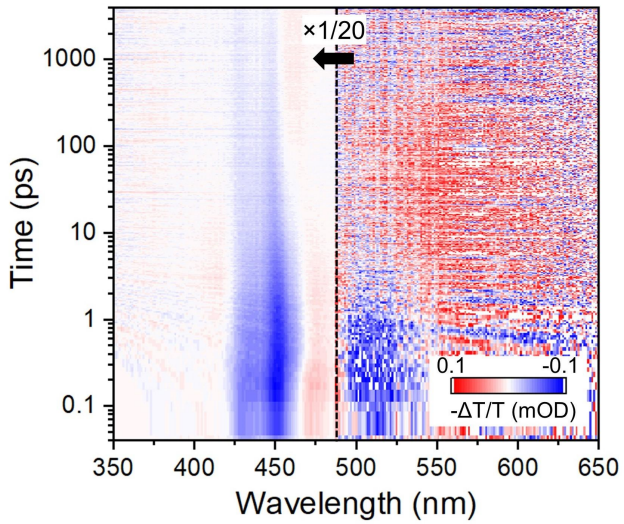

Figure S6. Room temperature transient absorption of $[AgSePh]_\infty$ single crystal. The single crystal shows a photoinduced absorption band around 550 nm as well. Pump wavelength 430 nm, pump energy 0.004 μJ pump energy (about 8.5 μJ/cm^2 due to different probe spot size compared to all other TA measurements on extended $[AgSePh]_\infty$ films).

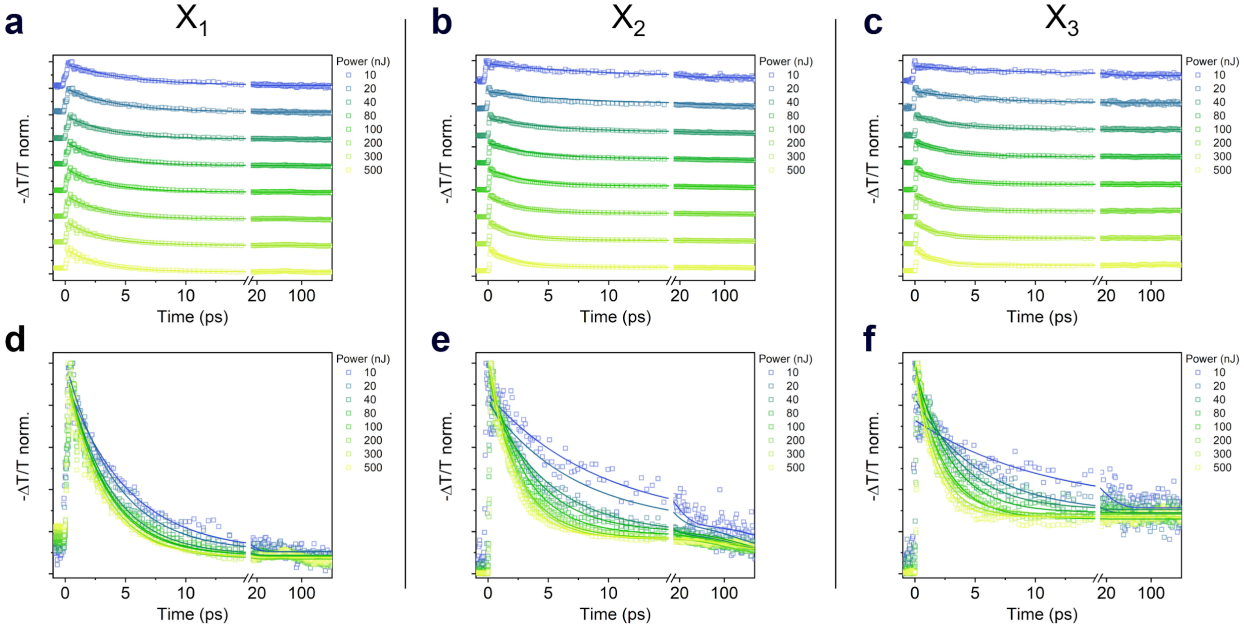

Figure S7. Transient absorption dynamics obtained by pumping at 429 nm, restricted to the negative signals at selected wavelengths, each representing the evolution of excitonic transitions. **a,** and **d,** X_1, 456 nm. **b,** and **e,** X_2, 447 nm. **c,** and **f,** X_3, 427 nm. T = 77 K.

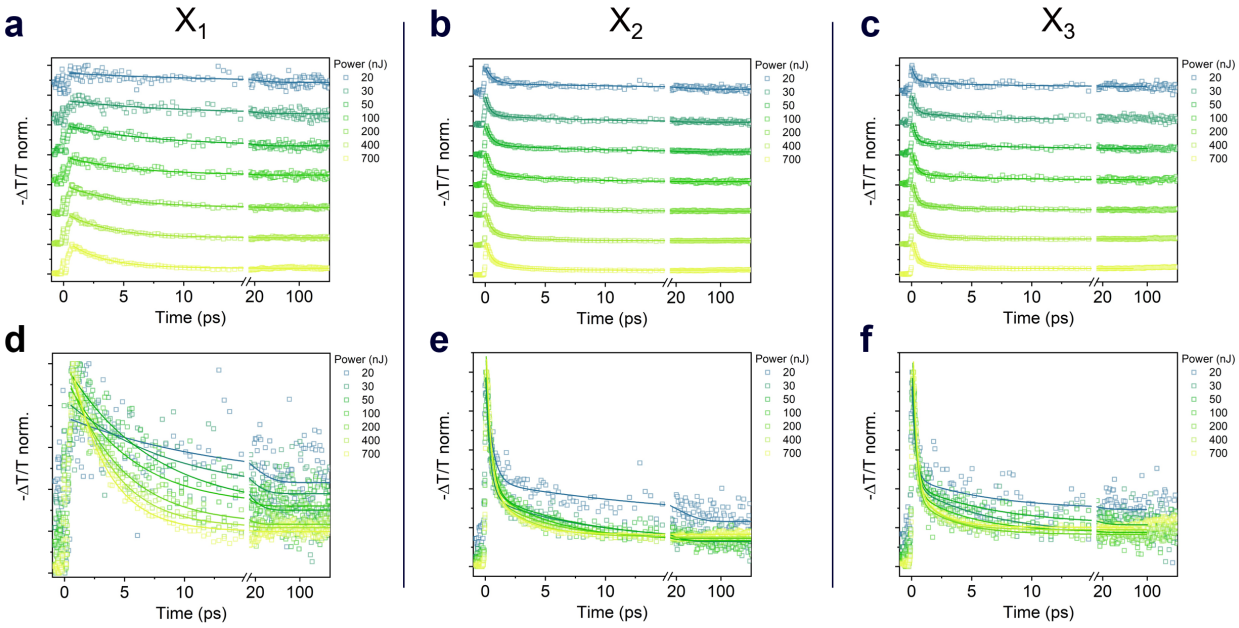

Figure S8. Transient absorption dynamics obtained by pumping at 330 nm, restricted to the negative signals at selected wavelengths, each representing the evolution of excitonic transitions. **a,** and **d,** X_1, 456nm. **b,** and **e,** X_2, 447 nm. **c,** and **f,** X_3, 427 nm. T_{bath} = 77 K.

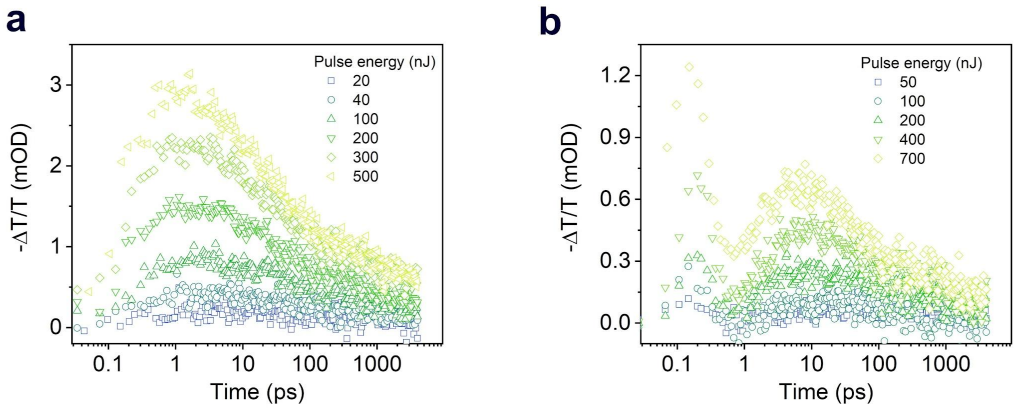

Figure S9. PIA transient absorption signals at 550 nm at different pump fluences. Pump wavelength **a,** 429 nm and **b,** 330 nm. T = 77 K.

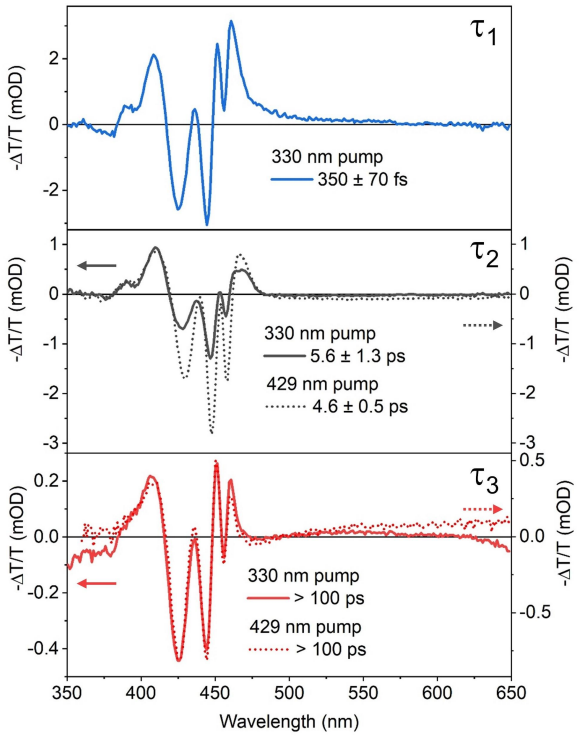

Figure S10. Global fit analysis of transient absorption dynamics. The different panels show the different exponential time scales (τ_1,τ_2,τ_3) and the corresponding spectra extracted from a global fit analysis for free carrier pumping (pump wavelength 330 nm, solid lines) and resonant excitonic pumping (429 nm, dashed lines). For free carrier pumping, an initial ultrafast relaxation takes place (top panel, τ_1 = 350 fs), which is absent for excitonic pumping . The intermediate time scale (τ_2 ~ 5 ps) is governed by exciton trapping, with similar spectral signatures, but increased bleaching for excitonic pumping (middle panel). On long time scales (τ_3 > 100 ps), the response is governed by a heated phonon bath, which is the same for free carrier and excitonic pumping. Pump wavelengths 330 nm and 429 nm have pump energies 0.1 μJ and 0.04 μJ, respectively. *T* = 77 K.

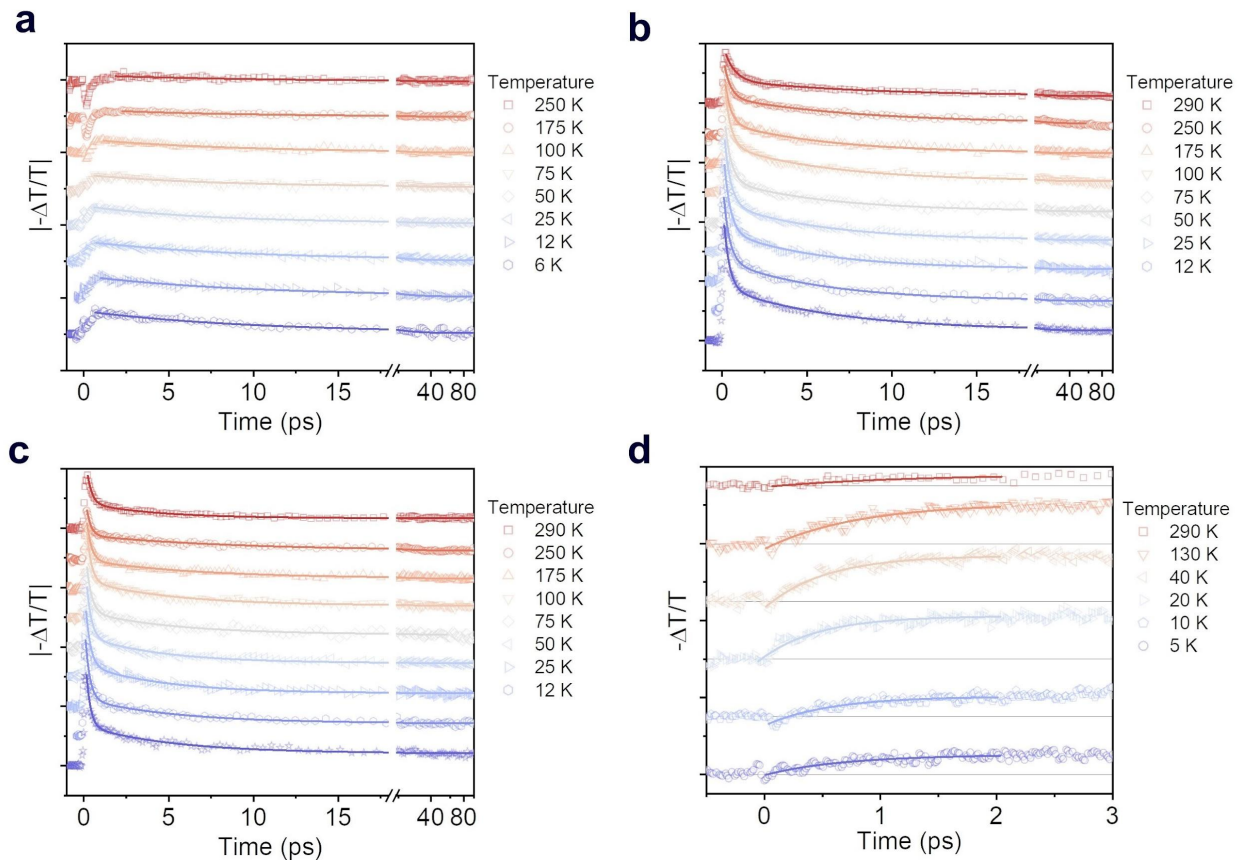

Figure S11. Exciton dynamics over temperature. **a-c,** Free excitons decay signals for X_1 **(a)**, X_2 **(b)**, X_3 **(c)**, pump wavelength 330 nm, pump energy 0.02 µJ. **d**, Self-trapped exciton rise (evaluated at 550 nm), pump wavelength 425 nm, pump energy 0.1 µJ.

Modelling of transient absorption data and lineshape analysis

To quantitatively model the transient absorption data, we employed the following workflow. First, we modelled the steady state absorption spectrum using generic oscillator functions $g(E, A, E_0, \sigma, \ldots)$ and a least-square fitting procedure, which in turn yields information about strength A, spectral position E_0, width σ, and other parameters of the involved transitions. Second, we defined modified versions of these oscillators $g(E, A + dA, E_0 + dE_0, \sigma + d\sigma, \ldots)$, where for example the spectral centers, weights, and widths are slightly shifted due to the pulsed optical excitation. The transient response is then modeled as the difference $g(E, A, E_0, \sigma, \ldots) - g(E, A + dA, E_0 + dE_0, \sigma + d\sigma, \ldots)$. Figure XXX shows the reference steady state absorption spectrum of $[AgSePh]_\infty$ recorded at a temperature of 77 K.

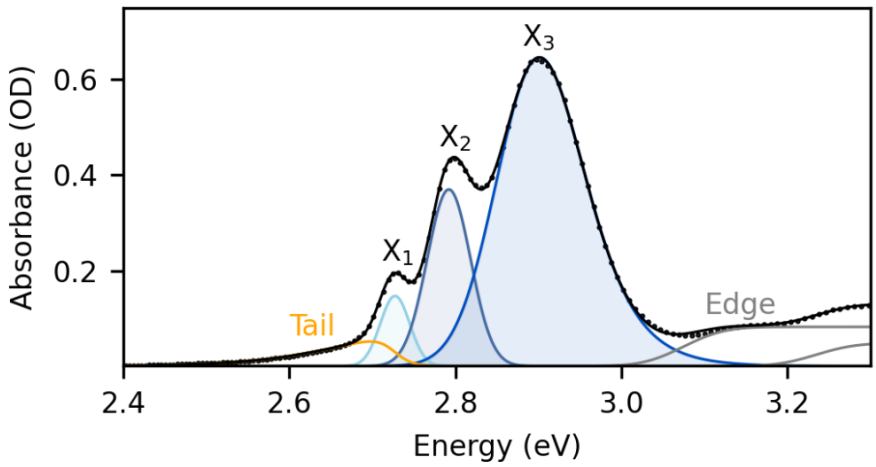

Figure S11. Modelling of steady state absorption. Three excitonic transitions X_1, X_2 and X_3 can clearly be discerned. X_3 exhibits an asymmetric line shape. Two steplike absorption onsets above 3.0 eV and low energy tail below X_1 can further be identified.

For the description of X_1 and X_2, we found that Gaussian line shapes yield the most consistent results. We used

$$g_{X1/X2}(E) = A/\sqrt{2\pi\sigma^2}\, e^{-(E-E_0)^2/(2\sigma^2)}$$

where *A* denotes the integrated spectral weight, E_0 the spectral center and σ the spectral width.

For the description of X_3, an asymmetric line shape with a high energy tail is required as can be seen from the absorption data. Here we used an exponentially modified Gaussian. Although the latter function is less often used in the context of line shape analysis, we found that it yields the numerically most stable results, in particular for the fitting of the transient absorption data. We used

$$g_{X3}(E) = A\gamma/2 \cdot e^{\gamma(E_0 - E + (\gamma\sigma^2)/2)} \cdot (1 - erf[(E_0 + \gamma\sigma^2 - x)/\sqrt{2\sigma^2}])$$

where *A* denotes the integrated spectral weight, E_0 the spectral center, σ the spectral width of the Gaussian, and γ the width of the high energy tail.

We furthermore introduce phenomenological step functions to model the observed absorption edges

$$g_{Edge}(E) = A\,(1 + erf[(E - E_0)/\sigma)]/2$$

where *A* denotes the amplitude, E_0 the spectral center, σ the spectral width of the absorption step.

As a last feature, we introduce a sigmoid function to describe the low energy tail of the steady state absorption close to X_1

$$g_{Tail}(E) = A \cdot [1/(1 + e^{-(E-E_0+S_1/2)/S_2})] \cdot [1 - 1/(1 + e^{-(E-E_0-S_1/2)/S_3})]$$

where A denotes the amplitude, E_0 the spectral center, and S_1, S_2, S_3 are the width parameters of the sigmoid.

Table XXX summarizes the fit parameters for the steady state absorption spectrum, the errors estimated from the covariance matrix, the initial values as well as the lower (upper) bounds of the parameters. Some parameters were fixed (*Vary* was set to *False*) to improve convergence of the model. For the fitting we used python in conjunction with the package lmfit to construct the fit models. As the minimization routine for the constrained model, we used *least_squares* from the scipy.optimize package.

Parameter	Fit value	Abs. error	Rel. error	Initial	Low. bound	Up. bound	Vary
A_{X1}	0.00655	1.59e-04	(2.44%)	0.018	0.	1.0	True
E_{X1}	2.727	0.0026	(0.10%)	2.728	2.7	2.80	True
σ_{X1}	0.0177	3.21e-04	(1.81%)	0.015	0.0	0.03	True
A_{X2}	0.0242	2.62e-04	(1.08%)	0.09	0.0	1.0	True
E_{X2}	2.792	1.76e-04	(0.01%)	2.793	2.78	2.81	True
σ_{X2}	0.0261	2.13e-04	(0.82%)	0.026	0.0	0.20	True
A_{X3}	0.0901	1.97e-04	(0.22%)	0.154	0.0	1.00	True
E_{X3}	2.872	2.22e-04	(0.01%)	2.902	2.80	2.95	True
σ_{X3}	0.0451	2.93e-04	(0.65%)	0.07	0.0	0.20	True
γ_{X3}	25.0	0.26	(1.06%)	23	0.0	100.0	True
A_{Tail}	0.094	0.0021	(2.26%)	0.01	0.0	1.0	True
E_{Tail}	2.70	0.000	(0.00%)	2.7	2.60	2.72	False
S_1	0.05	0.00	(0.00%)	0.05	0.0	0.20	False
S_2	0.061	0.0017	(2.87%)	0.05	0.0	0.20	True
S_3	0.0103	0.0108	(96.57%)	0.01	0.0	0.05	True
A_{edge1}	0.0823	0.0	(0.00%)	0.082	0.00	2.0	False
E_{edge1}	3.084	0.0013	(0.04%)	3.075	3.0	3.50	True

σ_{edge1}	0.055	0.0	(0.00%)	0.055	0.0	0.06	False
A_{edge2}	0.048	9.85e-04	(2.05%)	0.048	0.0	2.0	True
E_{edge2}	3.2343	0.002	(0.06%)	3.229	3.20	3.50	True
σ_{edge2}	0.052	0.0037	(7.21%)	0.05	0.0	0.20	True

In the next step, we modelled the transient absorption data as

$$\Delta T/T \;=\; \sum g(E,\, A,\, E_0,\, \sigma,\, \ldots) \;-\; g(E,\, A \,+\, dA,\, E_0 \,+\, dE_0,\, \sigma \,+\, d\sigma,\, \ldots)$$

Additionally, we introduce a Gaussian peak to describe the broad signature of the self-trapped exciton, which is not present in the transient absorption data.

$$g_{STE}(E) \;=\; A/\sqrt{2\pi\sigma^2}\, e^{-(E-E_0)^2/(2\sigma^2)}$$